

The Promise and Limitations of Precision Gravity: Application to the Interior Structure of Uranus and Neptune

NAOR MOVSHOVITZ¹ AND JONATHAN J. FORTNEY¹

¹*Department of Astronomy and Astrophysics, University of California, Santa Cruz, California,
95064 USA*

ABSTRACT

We study the constraining power of a high-precision measurement of the gravity field for Uranus and Neptune, as could be delivered by a low periapse orbiter. Our study is practical, assessing the possible deliverables and limitations of such a mission with respect to the structure of the planets. Our study is also academic, assessing in a general way the relative importance of the low order gravity, high order gravity, rotation rate, and moment of inertia (MOI) in constraining planetary structure. We attempt to explore all possible interior density structures of a planet that are consistent with hypothetical gravity data, via MCMC sampling of parameterized density profiles. When the gravity field is poorly known, as it is today, uncertainties in the rotation rate on the order of 10 minutes are unimportant, as they are interchangeable with uncertainties in the gravity coefficients. By the same token, when the gravity field is precisely determined the rotation rate must be known to comparable precision. When gravity and rotation are well known the MOI becomes well-constrained, limiting the usefulness of independent MOI determinations unless they are extraordinarily precise. For Uranus and Neptune, density profiles can be well-constrained. However, the non-uniqueness of the relative roles of H/He, watery volatiles, and rock in the deep interior will still persist with high-precision gravity data. Nevertheless, the locations and magnitudes (in pressure-space) of any large-scale composition gradient regions can likely be identified, offering a crucially better picture of the interiors of Uranus or Neptune.

1. INTRODUCTION

The gravity field of a giant planet is perhaps our best window into its interior structure and composition. Obtaining gravity data is no simple task though. Rough estimates can be deduced with ground-based observations of natural satellites, but

precise determinations must come from tracking radio signals from probes sent to the outer solar system to orbit, or at least fly by these worlds. Turning the hard-won gravity data into inferences about a planet’s interior is also not a straightforward task. There is no simple inversion; the usual process involves creating models of the planet’s interior and deducing features of the planet we are interested in, for example the existence and size of a heavy element core, based on how well the calculated gravity of model planets with such features matches the observed gravity of the real planet.

The past decade has seen the *Juno* Mission to Jupiter and the *Cassini* Grand Finale orbits at Saturn revolutionize our understanding of these planets as the precision of the gravity fields of these giant planets have improved by two orders of magnitude (Bolton et al. 2017; Iess et al. 2018, 2019; Durante et al. 2020). The bulk compositions of these planets are dominated by hydrogen and helium, and the typical questions involve the mass and distribution of heavy elements within the planets, to better understand structure, formation, and evolution. Since these data have revolutionized our views of Jupiter and Saturn (Stevenson 2020; Mankovich & Fuller 2021), it is a natural question to wonder how similar data may be able to alter our views of Uranus and Neptune. A variety of orbiter mission concepts have been put forward with comprehensive science cases, including improving our view of the interior structure of these planets (Hofstadter et al. 2019; Fletcher et al. 2020; Rymer et al. 2021).

The advances in giant planet gravity field data have necessitated advances in modeling efforts, first in terms of new methods of ultra-precise gravity field calculations (Hubbard 2012, 2013; Nettelmann 2017; Nettelmann et al. 2021). A second effort has been in re-examining assumptions that go into models. What may not be well appreciated are the host of assumptions that typically go into models, making virtually every inference about a giant planet’s structure strongly model dependent.

1.1. *The role of gravity in interior models*

Physical interior models try to create a self-consistent description of the composition, density, pressure, and temperature, at every point inside the planet. Gravity enters the problem from the requirement of hydrostatic equilibrium, connecting the pressure p (really its gradient) and density ρ at every point. Hydrostatic equilibrium also allows us to use a one dimensional structure, $\rho(s)$ and $p(s)$, where s is the mean (volume equivalent) radius of a surface of constant density and pressure¹. Once a self-consistent $\rho(s)$ is determined, it can be integrated to yield a total planetary mass, radius, and external gravity field which can be compared with observed values to judge the model’s overall likelihood. For the planets Uranus and Neptune, a recent reference in the physical picture is Nettelmann et al. (2013).

¹ The existence of surfaces of constant density and pressure is also guaranteed by the condition of hydrostatic equilibrium.

The gravitational potential exterior to the planet, $V_e(\mathbf{r})$, is described by the expansion

$$V_e(\mathbf{r}) = -\frac{GM}{r} \left(1 - \sum_{n=1}^{\infty} (a_0/r)^{2n} J_{2n} P_{2n}(\cos \theta) \right), \quad (1)$$

the connection with the interior mass distribution is in the coefficients

$$J_n = -\frac{1}{Ma_0^n} \int \rho(\mathbf{r}') (r')^n P_n(\cos \theta') d\tau'. \quad (2)$$

In this expansion M is the planet’s mass, a_0 is a normalizing constant with dimensions of length, commonly a whole number of kilometers close to the planet’s equatorial radius, and P_n are the Legendre polynomials. The integrals are carried over the volume of the planet.

Equation (1) depends on the co-latitude angle θ but not on azimuth, and is also strictly north-south symmetric (even n only). Clearly, this is an approximate, partial description of the full gravity field. Furthermore, the integrals (2) require knowledge of the equilibrium shape of the model planet. Methods for deriving this shape (sec. 2.3) rely on equilibrium between gravitational and centrifugal *potential*, which greatly restricts the rotation state under consideration. In fact rigid rotation at a constant rate ω is almost always assumed. Real planets, on the other hand, exhibit more complex gravity. Non-zero odd gravity harmonics ($J_{3,5,7,9}$) have been measured for Jupiter (Iess et al. 2018) and used to infer the depth of the observed asymmetric surface flow (Kaspi et al. 2018). And in Saturn evidence for strong differential rotation was found not in the odd J s but rather in the unexpected magnitude of even harmonics higher than J_6 (Iess et al. 2019; Galanti et al. 2019).

There is no doubt that such non-hydrostatic effects can be expected to exist in Uranus and Neptune too. Nevertheless it is appropriate to focus on the simpler gravity field with the implied uniform rotation as these are the most important for determining the bulk structure of the interior. We discuss nonuniform rotation again in sec. 2.5 but in the rest of the text “gravity” implies the zonal, north-south symmetric gravity of eq. (1).

1.2. The role of the equation of state

Pressure and density are also related via a thermodynamic equation of state (EOS). A self-consistent solution is found, by iteration, such that the value of pressure satisfying hydrostatic equilibrium, which depends on gravity, matches everywhere the value given by the EOS. The EOS requires knowledge, at every point, of temperature and composition. Temperature can be calculated by equations of heat transfer, perhaps with input from *cooling models* that follow a long-term evolution of the planet. In detailed *structure models* a prescribed, static temperature structure (usually adiabatic) or, equivalently, entropy structure is used. Composition cannot be calculated by an equation; it must be stipulated.

And that fact regarding composition is a limitation: the model must assume the very thing it is supposed to infer. To be sure, there are some very good assumptions

that one can make. For example, if the target planet is a gas giant we may assume that, in a large fraction of the volume of the interior, the dominant species is a mix of hydrogen and helium, although the relative proportion of hydrogen to helium should be allowed to change with depth, given helium phase separation (Stevenson & Salpeter 1977; Mankovich & Fortney 2020).

In the case of the ice giants, on the other hand, the dominant species is not so easy to guess. Relatively recent models within the physical picture (Nettelmann et al. 2013) suggest important roles for H/He, water and other volatiles, as well as rock/iron. Some models even suggest more rock than volatiles (Teanyby et al. 2020). Some of the most important questions about planet formation (that are perhaps the main motivation for the model in the first place) depend most strongly on the inferred content, composition, and distribution of heavier elements, with this “metals” mass fraction referred to as $Z(s)$. Recent reviews can be found in Helled et al. (2020) and Helled & Fortney (2020). Whereas for Jupiter and Saturn the outcome of the inferred $Z(s)$ is not overly sensitive to exactly *which* heavy element (i.e., volatiles vs. rocks) one uses in the model, the same is *not* true for Uranus and Neptune.

However, such a hypothetical model is already much too complex. To resolve the interior to a meaningful degree requires discretizing the continuous variables on a fine grid in s , with at least hundreds and preferably thousands of grid points, resulting in thousands of model parameters and an impracticable task. Some very strong simplifying assumptions are needed. The most important one is the assumption of some kind of layering.

The most common class of models, for both the gas giants and ice giants, has for a long time been the three-layer model. The planet is assumed to consist of radial regions, each of homogeneous composition. This assumption is made typically for computational expediency and potentially out of physical reasoning, the latter being that thermodynamics may support, under some conditions, the existence of fully convective regions, with boundaries between them that resist mixing (Bailey & Stevenson 2021). Of course, that thermodynamics may support such configurations is no proof that these are the only possible ones. Modelers have been gradually increasing the sophistication of layered-composition models, for example by adding layers of composition gradients, and will no doubt continue to do so, while still retaining the basic paradigm. Figure 1 shows what density profiles deriving from such models of Uranus and Neptune (Nettelmann et al. 2013) may look like; the three-layer structure is clearly visible.

1.3. *Composition agnostic models*

An alternative approach that has been used is to create so-called *empirical* models. Rather than parameterize the planet’s composition and then solve for the pressure and density structure, these models parameterize the structure directly and make inferences about the composition from the resulting models (Helled et al. 2009, 2011a;

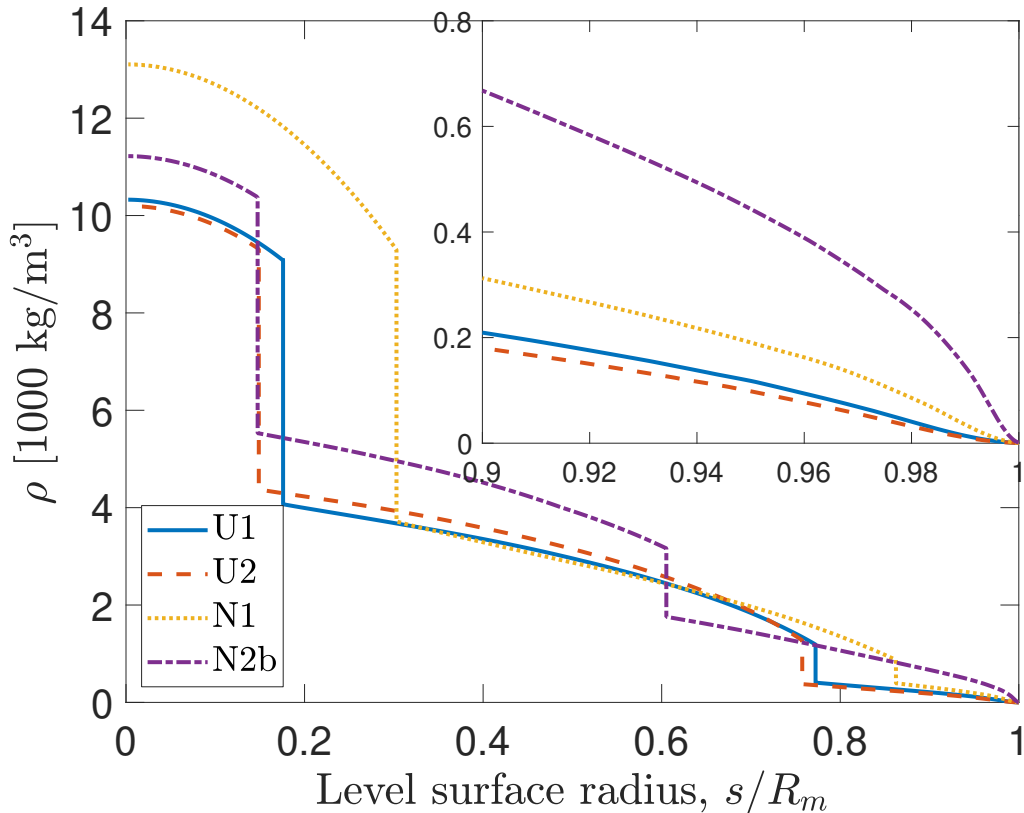


Figure 1. Density profiles $\rho(s)$, of the three-layer models of [Nettelmann et al. \(2013\)](#), re-plotted from their data. R_m is the mean (volume equivalent) radius of a surface of constant density, which by hydrostatic equilibrium must also be a surface of constant pressure and potential; s_0 is the mean radius of the 1-bar surface.

[Movshovitz et al. 2020](#)). For example, some models may assign a synthetic (and simple) pressure-density relation to one or more regions of the planet. A popular choice is a combination of one or more polytropic regions, where $p(s) \propto \rho(s)^{1+\frac{1}{n}}$ for polytropic index n , and perhaps a region of constant density approximating a core ([Neuenschwander et al. 2021](#)). A synthetic pressure-density relation can be used just like a physical EOS to derive self-consistent equilibrium shape and density profiles. A three-layer structure like those shown in [fig. 1](#) can be approximated by using three different polytropes in three radial regions.

The density profile can also be parameterized directly, and this is our preferred approach here. A parametric mathematical representation of a curve is chosen, mapping a vector of parameter values $\mathbf{x} \in \mathbb{R}^n$ (hopefully n is not too large) to a density profile $\rho(s)$ and thereby, through hydrostatic equilibrium, to a self-consistent interior structure. The advantage of being entirely divorced from an assumed equation of state, real or synthetic, is that density profiles representing both layered composition as well as continuous composition can be represented with the same model. The disadvantage is that without an EOS, real or synthetic, to guide us, it is harder to

know how to interpret the resulting density profile. Our work builds on pioneering work in this area, of “random” interior models of Uranus and Neptune (Marley et al. 1995; Podolak et al. 2000), that were motivated by an exploration to move past the 3-layer model and explore the widest possible range of density distributions allowed by the gravity field.

1.4. *Nonuniqueness of models*

Regardless of how a model planet is constructed, with a physical EOS, a synthetic EOS, or a synthetic $\rho(s)$, there remains the problem of degeneracy of solutions. The problem is, simply, that multiple models can be constructed that all match the measured gravity field to within a specified uncertainty. In fact there are infinitely many such models, covering an unknown region of parameter space. When modelers claim to constrain some desired property of the planet, for example if they say that the heavy element content of the planet is found to be between some upper and lower bounds, what they mean is that, given their chosen model design, no solutions were found with heavy element content outside those bounds, that match the gravity measurement to within some tolerance. It is typically not known how much of this constraint is due to the measured or observed properties of the planet and how much is due to the assumptions built into the model, or even to incomplete exploration of the model parameter space.

That is the main deficiency we aim to address in this work. Focusing on Uranus and Neptune as the target planets, we choose a parameterization designed for maximum flexibility and a sampling method designed for maximum coverage, and generate representative random samples of $\rho(s)$ from several different distributions, each constrained by a different combination of observable planetary properties. Concretely, we constrain the $\rho(s)$ distributions by applying progressively stronger information as follows: (1) The planet’s mass and radius only; (2) Mass, radius, and rotation period; (3) Also adding the planet’s J_2 and J_4 gravity coefficients, with uncertainty varying from that of currently available data to precision limited only by computational considerations; (4) With nominal values of gravity coefficients of increasing order (up to J_{12}), hypothetically, as if known to great precision.

The difference between distributions of density profiles obtained with the different constraints illustrates the “constraining power” of the different observables.

Our focus on Neptune and Uranus here is motivated by a number of factors. Compared with the gas giants, Jupiter and Saturn, the vital observables of the ice giants, including and especially their gravity fields and rotation periods, are much less well known. A future mission to these worlds with one of the goals being to obtain more precise measurements of their gravity fields would be extremely valuable, this is not in doubt. What is still unknown, however, is what would be the expected relationship between the precision of such measurements and our ability to translate them into better constraints of the interior structure of Uranus and Neptune. Our work

here provides motivation for such missions and also a framework to understand their limitations, such that we can better assess whether and how a precision gravity field could revolutionize our view of these planets.

We explain in detail the methods of this experiment in sec. 2. Theoretical results are illustrated in sec. 3. Results specific to Uranus and Neptune, demonstrating the difference between models constrained with currently available data for these planets and data improved by a plausible mission scenario are shown in sec. 4. Our conclusions are summarized in sec. 5.

2. EXPERIMENTAL METHOD

2.1. Overview

In order to evaluate the potential of precise measurements of the gravity fields to improve our knowledge of the interiors of the ice giants we generate samples of interior density profiles that are constrained by successively higher-order and/or more precisely known gravity coefficients. By comparing the range of density values, and variety of density profiles attained by each sample we get an idea of the “constraining power” of gravity as a measured observable.

We start with a sample of density profiles guided by knowledge of the mass and radius of the planet only, to use as a baseline for comparison. The oblate shape of the rotating planet is calculated because it affects the mass, but the associated gravity field is not expected to match observation. Even so, the space of allowed $\rho(s)$ curves is already constrained by basic physics. Trivially, $\rho(s)$ must be monotonic strictly decreasing with s and its integral from the center to the surface should match the planet’s mass, within observational uncertainty. Additionally, the relationship between pressure and density in hydrostatic equilibrium implies $\lim_{s \rightarrow 0^+} d\rho/ds = 0$. By themselves these conditions only restrict the shape of the $\rho(s)$ curve, not its scale, but we can constrain the scale by putting reasonable limits on the density at both the surface and the center of the planet.

On the surface, which in our models we take to mean the 1-bar surface, we get a rough estimate of density by applying the ideal gas law to a protosolar mix of hydrogen and helium (mean molecular weight 2.319 amu) at the observed temperature, $T_{1\text{bar}}$. This leads to a nominal value of $\rho_{1\text{bar},U} = 0.367 \text{ kg/m}^3$ for Uranus, and for Neptune $\rho_{1\text{bar},N} = 0.387 \text{ kg/m}^3$. The 1-bar temperature itself is not a direct measurement. It is inferred from analysis of radio occultation data from the *Voyager 2* mission (Lindal 1992) and includes uncertainty of several percent. And of course the atmospheric composition is unknown. Combining the uncertainties from temperature and composition (mean molecular weight), we should allow some “play” in the 1-bar surface density, treating it as a sampled variable with an appropriate prior. However in preliminary samples we found that the resulting $\Delta\rho_{1\text{bar}}$ is too small to have any effect on the sample, and so we keep $\rho_{1\text{bar}}$ fixed in all models to speed up the sampling process.

Table 1. Reference planetary values

	Uranus	Neptune
G (10^{-11} m ³ kg ⁻¹ s ⁻²)	6.67430(15)	6.67430(15)
M (10^{24} kg)	86.8127(40)	102.4126(48)
a_0 (km)	25559	24764
$T_{1\text{bar}}$ (K)	76(2)	72(2)
P (sec)	62064(600)	57996(600)
J_2 ($\times 10^6$)	3510.7(7)	3536.5(47)
J_4 ($\times 10^6$)	-34.2(13)	-36.0(31)

NOTE—Reference values from [Tiesinga et al. \(2021, 2018 CODATA\)](#) and <http://ssd.jpl.nasa.gov>, analysis of Voyager data from [Lindal \(1992\)](#), rotation period from [Podolak & Helled \(2012\)](#), and J_n values from [Jacobson \(2009, 2014\)](#) renormalized to fixed value of a_0 .

The density at the center of the planet is, of course, not directly available. We can estimate a reasonable upper bound value by considering the order of magnitude of the central pressure. We set the upper limit for both planets at 20,000 kg/m³, comfortably above the density of pure rock at 50 Mbar.

The rotation period of the planets is also not precisely known. ([Jacobson 2009, 2014](#); [Helled et al. 2010](#); [Podolak & Helled 2012](#); [Nettelmann et al. 2013](#)). For a given density profile, changing the rotation period will change the equilibrium shape and, as the equatorial radius is held fixed, also the mass and gravity. We therefore include the rotation period as one of the sampled parameters, with an estimated prior, allowing the MCMC procedure to sample from the space of density profiles and rotation period simultaneously. The effect of rotation period uncertainty is discussed further in sec. 3.

To summarize: the baseline sample, for each planet, is drawn from the space of one dimensional profiles restricted to monotonically decreasing $\rho(s)$ with vanishing $d\rho/ds$ at the center and satisfying $\rho(s_0) = \rho_{1\text{bar}}$ and $\rho(s) \leq \rho_{\text{max}}$ everywhere. The prior includes information about the imperfectly known rotation period, and the likelihood function driving the sampling procedure compares the integral of the density profile with the planet’s reference mass M . More detail about the exact sampling procedure is given in the appendix. The values used for these baseline models are summarized in Table 1.

We then proceed to constrain the interior density profiles further by using additional information about the planet’s gravity field. Currently, approximate determination of the gravity fields of Neptune and Uranus comes from a combination of ground based astrometry and radio data from both *Voyager* missions ([Jacobson 2009, 2014](#), and references therein). Gravity harmonics J_2 and J_4 are available, with significant

uncertainty, for both planets. We use the nominal values from Table 1 to center the multidimensional Gaussian we use in the sampling likelihood function,

$$D_J^2 = \sum_{\text{even } n}^{n_{\max}} \left(\frac{J_n - J_n^{\text{obs}}}{\sigma_{J_n}} \right)^2. \quad (3)$$

But for the σ_{J_n} uncertainties we are less interested in the precision of the *Voyager* missions data; our question is the theoretical constraining power of increasingly precise gravity. We assign, in different samples, $\sigma_{J_n}/J_n = 10^{-\mu_n}$ with μ_n ranging from 2 to 6. Concretely, we obtained samples where n_{\max} was 2, 4, 6, and 12. For $n_{\max} > 4$ we do not have measured nominal values for the Gaussian centers; we use the mean values from the sample with $n_{\max} = 4$.

Comparing samples obtained with $n_{\max} = 2$ but with varying values of uncertainty, σ_{J_2} , will show the expected benefit of more precise measurements of the low-order coefficients. Comparing samples obtained with increasing n_{\max} and fixed σ_{J_n} will show the expected benefit of measuring higher-order coefficients, even crudely. Comparing samples obtained with the same n_{\max} and σ_{J_n} but different priors set on rotation period will show the expected benefit of more precise determination of rotation. In a real mission, of course, these are not distinct, independent measurements. Nevertheless, knowing which of the above options provides the most benefit, in terms of constraining models of interior structure, may help optimize the mission design.

Before we look at the resulting sample distributions we need to define the density profile parameterization used in this work.

2.2. Parameterization of the density profiles

Consider the density profiles of the three-layer Uranus and Neptune models of [Nettelmann et al. \(2013\)](#), shown in Figure 1. These profiles are derived from models that solve the planetary structure equations for an assumed layered composition, using physical equations of state. Our goal is to find a suitable direct parameterization of density as a function of radius, $\rho(s)$, that is capable of capturing the profiles of Fig. 1 as a subset and is otherwise as flexible as possible. It is also important to keep the number of parameters small and, even more important, to minimize parameter correlations. The more parameters we use and the stronger the correlations between them, the longer it will take any sampling algorithm to adequately cover the sample space.

With these requirements in mind, what are the important features of the curves in Fig. 1 that we need to allow for? Each $\rho(s)$ curve is smooth and monotonic, except for two sharp discontinuities. In the physical models these discontinuities are “built-in”; the models assume layers of homogeneous composition with sharp boundaries between them. Three-layer models thus have two density discontinuities, the implicit assumption being that regions of composition gradients of length scale below the model’s resolution separate the layers. The smoothness of the $\rho(s)$ curve between

these density “jumps” suggests that the entire profile can be well-represented by a piecewise-polynomial function. Such a parameterization was used successfully in [Movshovitz et al. \(2020\)](#) to generate density profiles for Saturn, but here we utilize an alternative parameterization that is superior to the piecewise-polynomial in two significant ways, both having to do with representing the density jumps.

There are two important limitations to representing $\rho(s)$ with piecewise-polynomials. The first and more obvious is that this parameterization only allows for sharp density discontinuities, not gradual ones. There are two mathematical discontinuities (of the first kind) in every density profile, with parameters controlling their location, say fractions z_1 and z_2 of the planet’s radius, and jump magnitude, say δ_1 and δ_2 in density units². The jumps can merge ($z_1 \rightarrow z_2$) or one or both may vanish ($\delta_i \rightarrow 0$), but they cannot approximate a more gradual transition, a gradient region detectable on the scale of the model. These sharp density jumps are features of layered composition models and we want our parameterization to be able to reproduce them, but we would like it to have the flexibility to capture gradient regions as well, something that composition-based models have difficulty with.

The second limitation of the piecewise-polynomial parameterization is a technical one, that becomes apparent when we try to use MCMC algorithms to sample from the parameters’ joint posterior. It turns out that the parameters are very strongly correlated, leading to impractically long convergence time. One way to mitigate this problem is to fix values of the parameters z_1 and z_2 , obtain their marginal distributions by sampling the other parameter values under their conditional probability, and repeat the process for a range of reasonable values for z_i . A sample from the full posterior can be created by drawing from the marginal probabilities, in proportion to their relative likelihoods. While this approach provides a working method, it is more cumbersome and time consuming. Worse, the additional step of combining the marginals into a single posterior involves the difficult task of calculating, at least approximately, the *posterior odds* ratio (also called the Bayes factor or the evidence integral or, simply, the evidence). While this is a common and well-studied task, it still has no generally agreed upon best method ([Nelson et al. 2018](#)).

Our alternative parameterization represents $\rho(s)$ with a single continuous and continuously differentiable function:

$$\rho(z) = \rho(s/R_m) = \sum_{n=2}^8 a_n(z^n - 1) + \rho_0 + \sum_{n=1}^2 \frac{\sigma_n}{\pi} \left(\frac{\pi}{2} + \arctan(-\nu_n(z - z_n)) \right). \quad (4)$$

The first line is a degree-8 polynomial in $z = s/R_m$. It is constrained to have a vanishing derivative at $z = 0$ and to pass through the point $(1, \rho_0)$. Since we reference our J values to the 1-bar surface we take $\rho_0 = \rho_{1\text{bar}}$ to be the 1-bar density.

² For reasons of efficiency one may choose to use some one-to-one transformation of these parameters (e.g. [Movshovitz et al. 2020](#), Appendix B), but their physical meaning remains.

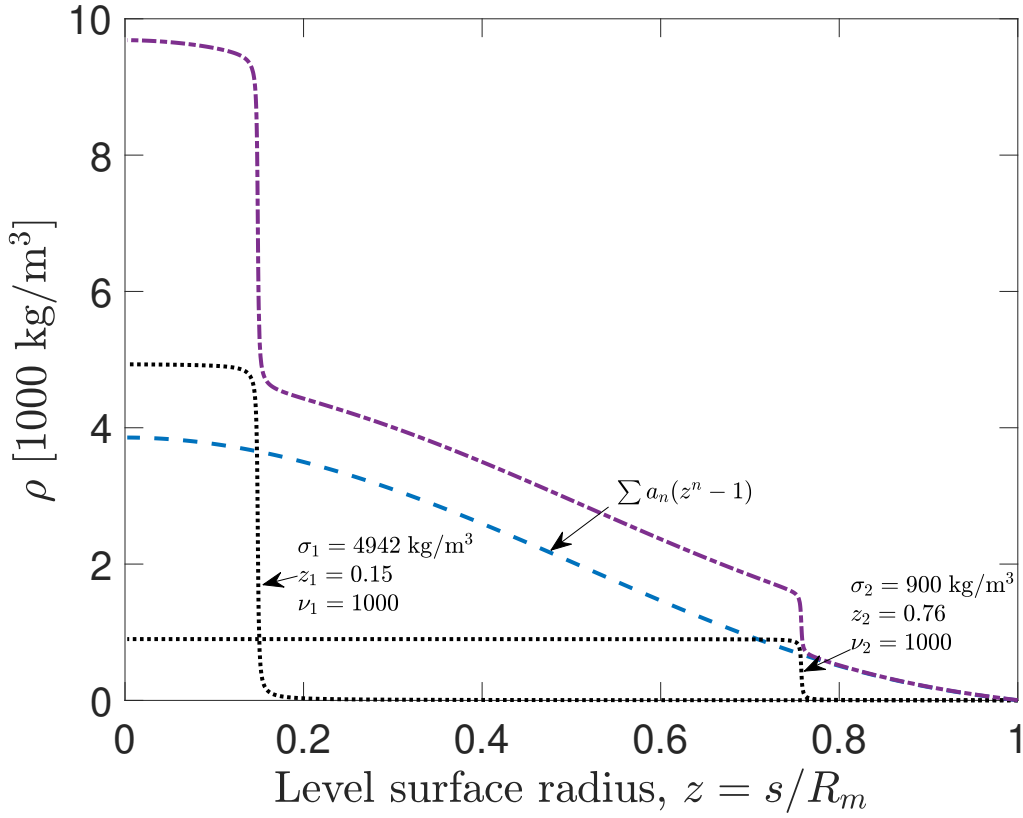


Figure 2. Illustration of the density parameterization used in this work. The dashed line is a degree-8 polynomial, the first part of eq. (4), constructed to match the surface density ρ_0 (a small but non-zero value) and have vanishing derivative near the center. The two dotted lines are the inner ($z_1 = 0.15$) and outer ($z_2 = 0.76$) Sigmoid functions of the second part of eq. (4). In this example both are approximating a sharp discontinuity ($\nu_1 = \nu_2 = 1000$), meaning the increase in density (σ_1, σ_2) happens over a short span. The dot-dashed line is the sum of the other three lines resulting in a density profile that matches the mass, radius, and low-order gravity of Uranus.

The second line in eq. (4) is a Sigmoid-function parameterization of possible density jumps, overlain on top of the polynomial. In this version of the parameterization we allow up to two such jumps. The parameter z_1 defines the location (in normalized radius) of the center of the inner of these. A density increase of σ_1 (in density units) is applied asymptotically and symmetrically around this point, the width being controlled by the non-dimensional sharpness parameter ν_1 . The jump can be made arbitrarily sharp, to resemble a discontinuity like the ones in Fig. 1, by increasing the value of ν_1 . Conversely, small values of ν_1 result in smooth, gradual density increase, indistinguishable from the background polynomial. The location, scale, and sharpness of the outer density jump are similarly determined by z_2 , σ_2 , and ν_2 , respectively. An example is illustrated in Figure 2, using parameter values tailored to approximate the shape of the Uranus model of [Nettelmann et al. \(2013\)](#).

2.3. Solving for equilibrium shape and gravity

There are several methods of calculating J_n for a model planet. They vary in theoretical precision and, more importantly, the precision they achieve *in practice* when working with manageable resolution (Hubbard et al. 2014; Wisdom & Hubbard 2016; Nettelmann 2017; Debras & Chabrier 2017; Nettelmann et al. 2021). In this work we use the Theory of Figures (ToF) algorithm, taken to 4th-order (ToF4) where possible and to 7th-order (ToF7) where necessary³. We estimate the practical precision of this method, when calculating the gravity of a given density profile (as opposed to a given density–pressure relation) with a given rotation period to have fractional error, $\sigma_{J_n}/J_n \approx 10^{-6}, 10^{-5}, 10^{-4}, 10^{-4}, 10^{-2}, 10^0$, for $n = 2, 4, 6, 8, 10, 12$, respectively. This estimate is derived by comparison with the extremely precise benchmark $n = 1$ polytrope gravity solutions of Wisdom & Hubbard (2016); they are the residual differences that remain when the ToF7 algorithm is applied to very high resolution models. We then choose the resolution of our models (the number, N , of discretized density levels) such that a doubling of N results in a relative difference to the resulting J_2 less than a part per million. We find that $N = 4098$ is always sufficient, and for consistency we use this resolution in all models in every sample, even when high precision is not required.

2.4. Sampling

As given in eq. (4) the number of parameters required to completely define the density profile is 13 (since we take ρ_0 to be constant). A degree-8 polynomial with two boundary conditions takes 7 parameters, and two potential density jumps take three parameters each (location, scale, and sharpness). Of course this polynomial-plus-Sigmoid parameterization can be made even more flexible, by increasing the polynomial degree and/or adding more Sigmoid terms. But the advantages of added flexibility must be carefully weighted against the cost of increasing the dimensionality of the sample space.

As it is, sampling from the 13-dimensional parameter space is a computationally expensive operation, although much less so than with the piecewise-polynomial parameterization. The advantage comes not from the number of parameters, which is similar in both, but from the weaker parameter correlations. The polynomial-plus-Sigmoid parameters are less strongly correlated, meaning a small change in one parameter while keeping the other parameters fixed results in a smaller overall change in the density profile. This significantly improves the behavior of the sampling algorithm. Even so, ensuring a large enough draw of independent samples with adequate coverage of the parameter space is not straightforward. We utilize the ensemble sampler algorithm of Goodman & Weare (2010) implemented in the `emcee` package (Foreman-Mackey et al. 2013) but we find it necessary to employ a “tempering” procedure, whereby sampling initially follows a modified loss function with arbitrarily lower sensitivity to parameter values to facilitate the algorithm moving through pa-

³ Simply because ToF7 is slower to run than ToF4.

parameter space, followed by sampling with the full loss function. Repeated application of this procedure results in a set of independent draws from what is hopefully the static but unknown posterior.

The full details of the sampling procedure are given in appendix (A).

2.5. *Some caveats*

The methodology described above was designed to minimize the impact of implicit assumptions and model limitations. Nevertheless, some necessary assumptions remain. Perhaps the strongest of these is the assumption, made throughout, of rigid rotation, in which every part of the planet is assumed to be moving at a single angular rotation rate ω . Many planets, including Uranus and Neptune, exhibit signs of non-rigid rotation but this does not always invalidate rigid-rotation models. Surface phenomena that involve only a small fraction of a planet’s mass would have negligible effect on the gravity field. But deeper rooted latitude- and depth-dependent motion will sufficiently change the equilibrium state at the time of measurement so that the observed gravity field’s coefficients are a mix of the rigid equilibrium gravity and non-rigid *wind* perturbations:

$$J_n^{\text{obs}} = J_n^{\text{rigid}} + J_n^{\text{wind}}. \quad (5)$$

We say perturbation, but for high order $J_{n>6}$ the non-rigid component (also referred to as the dynamic component) may be significant or even dominant. Models that assume rigid rotation to calculate J_n from a given density profile should be made to match $J_n^{\text{rigid}} = J_n^{\text{obs}} - J_n^{\text{wind}}$ instead of J_n^{obs} . Thus getting a solid handle on the non-rigid rotation’s contribution to the gravity field, at least its expected magnitude if not a nominal correction, should be considered a prerequisite to using J_n^{obs} to constrain interior models.

On both Uranus and Neptune, fast, east-to-west atmospheric streams are observed at cloud level; the crucial question being the depth of these winds. Analysis of the difference between J_4^{obs} and the J_4^{rigid} of relatively simple interior models suggests that these are relatively shallow jets, involving a small fraction of the planets’ mass (Kaspi et al. 2013), but the possibility remains that a better characterization of the gravity field will require addressing the correction due to dynamics. Work on this problem continues (Kaspi et al. 2017, 2018; Galanti & Kaspi 2017; Iess et al. 2018) and it is clear that without a good understanding of dynamic effects the usefulness of high-order gravity measurements would be much reduced.

A much more minor limitation comes from the use of composition-agnostic parameterization, which can theoretically generate $\rho(s)$ profiles that would be “unphysical” for one reasons or another, including characteristics that are difficult to predict or detect. It is not impossible, for example, that some density profile exist in the sample that if used with realistic equations of state to back out a temperature profile, would imply unrealistic temperature gradients somewhere in the interior. Any additional

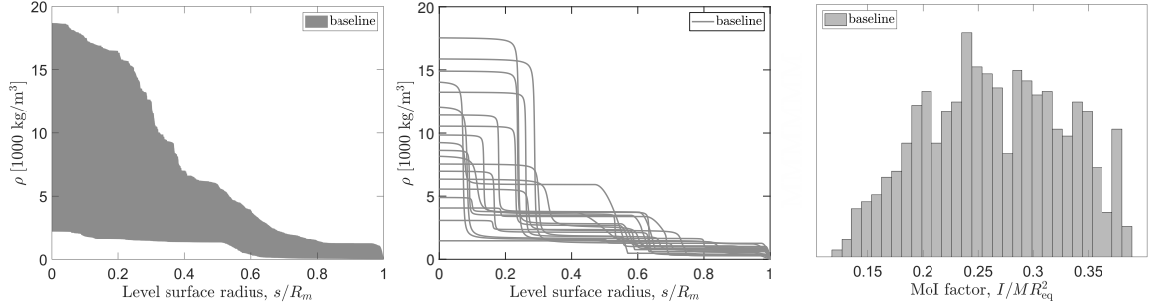


Figure 3. Three views of the baseline sample. Left: shaded region showing the range of density values, for each level surface mean radius s , between the 2nd and 98th percentiles of the sample; in effect the extent of the sample minus the occasional outlier. Middle: a subset of 20 density profiles from the sample, taken at equal intervals of percentiles of the central ($s = 0$) density values. Right: histogram of the moment of inertia factor, integrated while accounting for the equilibrium shape of level surfaces.

restriction of the parameterization that would guard against such features would be useful in further constraining the allowable models, but would necessarily rely on imperfectly known equations of state and/or additional model assumptions.

Conversely, the specific functional form (4), in addition to being possibly too permissive physically, may not be flexible enough mathematically. Certainly, it is *not* a complete basis for the space of all functions in $(0, 1)$ nor even for the more restricted space of functions representing a valid density profile. Just how much of that space may be “missing” is difficult to analyze. In section 3.1 we offer some reassurance, by examining a baseline sample, that the chosen functional form can indeed capture a very wide variety of density profiles.

Finally, any work that makes use of MCMC sampling must acknowledge that convergence to the correct static probability distribution is never assured. We describe in the appendix our sampling procedure and our reasons for accepting the resulting samples as correct.

3. CONSTRAINING POWER OF GRAVITY

3.1. A baseline sample

We begin by looking at the baseline sample. We will look at Uranus samples first, because we find it more instructive to examine different views of the same sample side-by-side, rather than compare the same view for both planets. Figure 3 shows three different views of the baseline Uranus sample. The left panel shows what we call the *envelope* view; a shaded area covering, for each radius, roughly a “two-sigma” spread in density values obtained there by the sample. This view is helpful in providing, at a glance, a sense of the overall extent of the density values reachable under the relevant constraint. Recall that for the baseline sample the only constraints were that each density profile integrates to the correct mass, with the boundary conditions $\rho(1) = \rho_0$ and $\rho(0) \leq \rho_{\max}$, and the Gaussian prior set on the rotation period (Table 1).

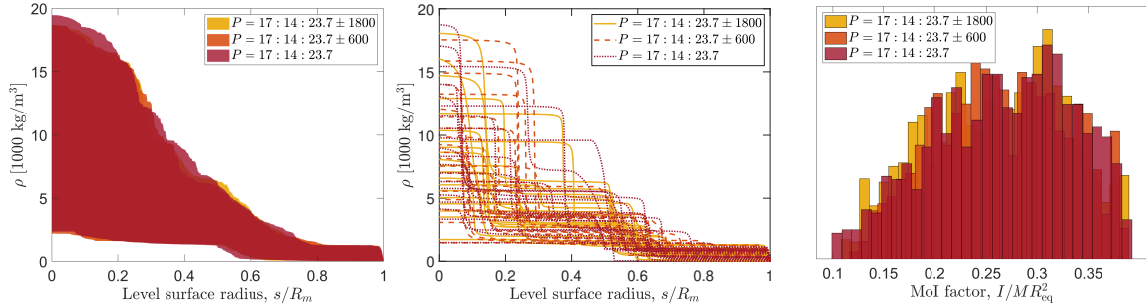


Figure 4. Same views as Fig. 3 showing samples obtained with large uncertainty (30 minute, light shade, solid lines), realistic uncertainty (10 minute, medium shade, dashed lines), and no uncertainty (dark shade, dotted lines) on the rotation period. The samples are essentially the same.

The middle panel of Figure 3 is what we call the *ensemble* view. A subset of 20 density profiles from the sample is shown, where we attempted to pick ones that show the variety of possible density profiles reachable under the given constraint. This view is more helpful for seeing features like the location and scale of density jumps and identifying regions of possible layering.

Lastly, the right panel is a histogram of the moment of inertia (MoI) values from the sample. As an integrated, scalar value, it serves as a quantitative measure of the “width” of the distribution.

The distribution of density profiles evident in the baseline sample is not surprising and does not contain much information about Uranus in particular or planetary interiors in general. Figure 3 is nevertheless important because, first, every other sample will be compared against the baseline in order to gauge the effectiveness of the employed constraints, and second, because it serves to validate the combination of the chosen parameterization scheme and sampling procedure. Recall that the goal was to have a parameterization flexible enough, and a sampling procedure robust enough, so that any restriction of the resulting density profiles evident in the sample can be attributed to the constraints that were deliberately used. The baseline sample was expected to, and in fact did cover essentially the entire range of plausible interior profiles. From panels (b) and, especially, (c) it is clear that both nearly “flat” profiles as well as very centrally condensed ones are reachable with this sampling method. Even if we cannot guarantee the exact shape of the probability distribution (it is possible, for example, that regions of apparent low probability would fill up gradually if much larger samples were drawn, see also appendix A) it is at least clear that the parameterization and/or sampling do not by themselves restrict the resulting samples.

3.2. Rotation period priors

A more precise determination of the rotation, by itself, is not a helpful constraint. In Figure 4 the baseline sample (rotation period a Gaussian prior with $\sigma = 10$ min, (Podolak & Helled 2012)) is shown again, overlain with two more samples. One obtained assuming much higher uncertainty in the rotation period (Gaussian prior,

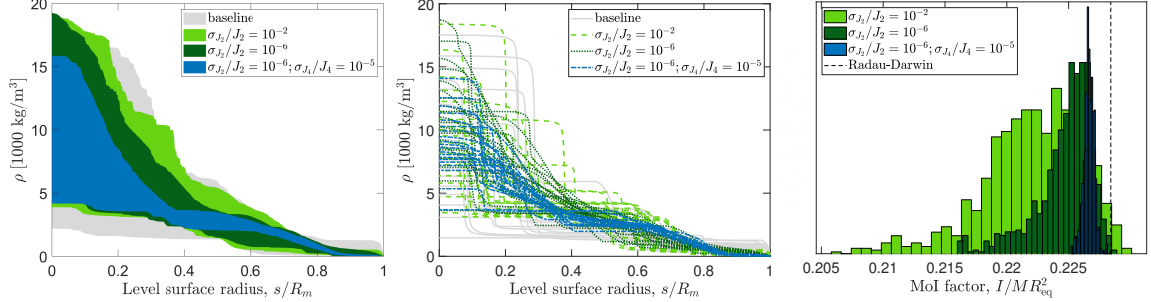


Figure 5. Same views as Fig. 3, showing samples constrained by J_2 , poorly known, J_2 precisely known, and J_2 and J_4 precisely known, in addition to the previous constraints of mass, radius, and rotation period.

$\sigma = 30$ min), and the second obtained with a perfectly known rotation period: the relevant parameter kept constant instead of being sampled.

It is perhaps surprising that these samples are essentially identical; that the rotation period can be varied by as much as an hour with apparently no effect on the shape of the allowable density profiles. This is because density and rotation are in a sense interchangeable, when the only observable used to constrain the sample is total mass. While faster rotation increases the planet’s oblateness which would result in a smaller mass for the same density profile (the outer mean radius is decreased since the equatorial radius is fixed), this is easily compensated by a small increase in density in the upper layers. It is possible that much stricter interior boundary conditions, i.e., much smaller ρ_{\max} and applying a central ρ_{\min} , would reveal the limits of allowable rotation period. We did not test this because there is no realistic prospect of independently estimating the central density.

We stress that even though the rotation period *by itself* is not a helpful constraint, it will become important when high-precision gravity is considered, in sec. 3.5.

3.3. Low order gravity

Adding information about the gravity field, even just a crudely estimated J_2 value, significantly shrinks the extent of allowable density profiles. Looking at Figure 5 we can deduce two important, if unsurprising lessons about the constraining power of gravity, and a third that was perhaps not as obvious *a priori*. The first is that gravity is most sensitive to the density structure at the outer regions of the planet, gradually becoming less sensitive the deeper we look, and almost indifferent to the density near the center of the planet. This behavior is well understood and easily predicted, at least qualitatively, from the definition of the gravity coefficients as integrals over the radius. Nevertheless we find it instructive to see a direct, quantitative illustration. This is most clearly seen in the left panel of Figure 5, while the middle and right panels better illustrate the second unsurprising fact, that gravity restricts the *shape* of the density better than its overall extent. For example, even the most restrictive sample, the one assuming very precisely known J_2 and J_4 (blue dash-dot lines in the figure), allows the central density to reach values almost as low or as high as the

less restrictive samples, or even the baseline sample. But there are many ways in which a $\rho(s)$ curve can reach those values, and some of these curves appear in the less restrictive samples and are notably missing from the last one. In particular, large and sharp density increases at large ($0.3 \lesssim s/R_m \lesssim 0.6$) radii seem to be disfavored or even disallowed by this nominal value of J_4 , thereby telling us, in this case, that Uranus is unlikely to have a huge rocky core.

The last, and least predictable lesson gleaned from Figure 5 is that, loosely speaking, it is better to know more J values than to know the same J value more precisely. This is probably best seen in the right panel, as well as in other samples, not shown here, with different combinations of J_n and σ_{J_n} . While not exactly surprising it is nevertheless not obvious why, for example, a four order of magnitude improvement in the precision of the J_2 value would, by itself, amount to only a modest shrinking of the allowed range of densities, density profiles, or MoI values.

3.4. High order gravity

There are at present no usable estimates of actual J_n values for either planet, for $n > 4$. To continue investigating the potential constraining power of high-precision, high-order gravity measurement we need to assign some hypothetical yet reasonable values to J_n and σ_{J_n} .

For nominal J_n values the only sensible choice is to use the mean values from the previous samples, specifically from the most constraining one obtained so far (blue, dash-dot curves in fig. 5). Only J_2 and J_4 values were used in the likelihood function driving the sampling algorithm, but all values of J_n are available after the fact. Figure 6 reminds us that the distributions of J_n values for different n are highly correlated, yet there is a range of allowable values that could be further restricted.

The usable precision of gravity data, the σ_{J_n} , is limited by the worst of three factors. The first is the expected accuracy of determination by a hypothetical future orbiter mission, should it become available. For this we can look to the recent successes of the radio science teams of the *Cassini* and *Juno* missions in reconstructing the gravity fields of Saturn and Jupiter, respectively, from the spacecraft accelerations deduced from Doppler shifts detected in the radio link between the spacecraft and tracking stations on Earth. We may take the exquisite precision obtained during those missions as best-case bound of what might be expected from a future Uranus/Neptune mission. But recall that this truly impressive precision applies to J_n^{obs} and not to J_n^{rigid} (eq. 5). The second factor therefore is the expected accuracy of a correction term, J_n^{wind} . It is hard to speculate what that correction would look like, although it's safe to assume it will come with attached uncertainty greater than the formal $\sigma_{J_n}^{\text{obs}}$.

The last limiting factor is the precision with which we are able to calculate the equilibrium shape and gravity of a model planet. It is unusual for a numeric computation to rival observational data in terms of poorer accuracy, but this is in fact the case here. For the high-order gravity samples we solve for equilibrium shape and gravity

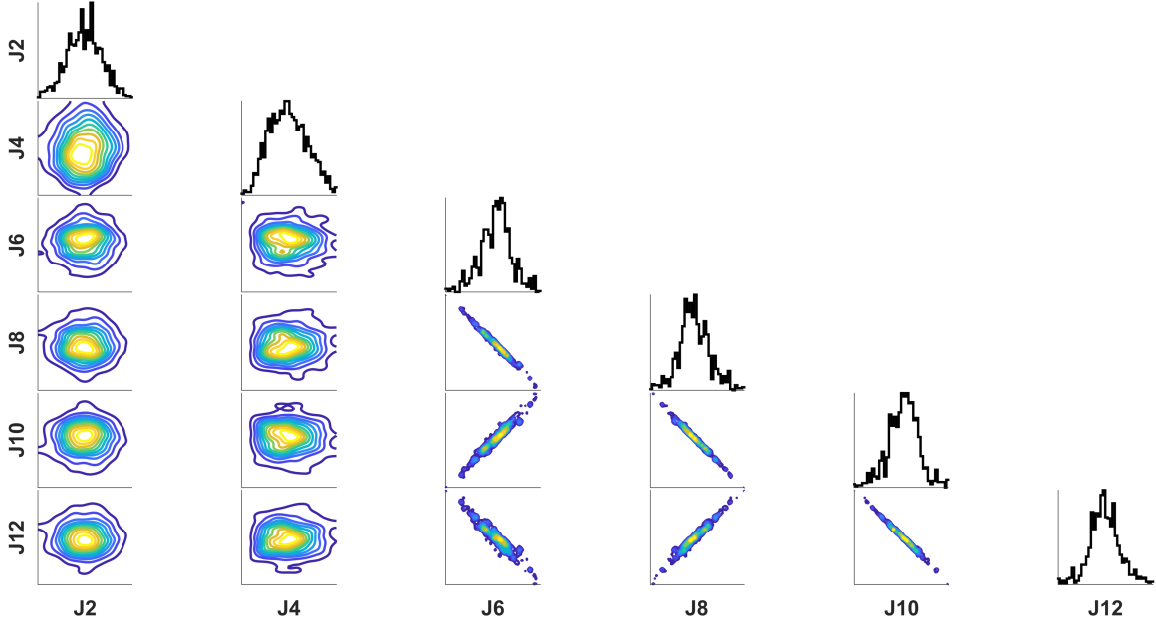


Figure 6. J values from an example MCMC run, illustrating correlations between J_n .

using the ToF7 method (sec. 2.3), which gives us usable values for up to J_{12} and the associated σ_{J_n} for the likelihood function.

With this framework, Figure 7 shows the distributions from samples constrained by progressively higher-order gravity, up to J_{12} . Again we see that high-precision gravity provides an excellent constraint on the density overall but cannot, by itself, pin down the central density or even the existence of a distinct central region of high density.

The moment of inertia factor seems to be very tightly correlated with the gravity, as soon as we go beyond J_2 . While correlation is expected, both gravity and MoI being essentially different integrals of the same $\rho(s)$, it has been suggested that an independent measurement of the MoI can provide new information, not already contained in the gravity field (Helled et al. 2011b; Helled 2011). It may be true that knowledge of J_n to any order and with full precision is equivalent to knowledge of $\rho(s)$, and therefore of every other quantity derived from it. Whether or not this is strictly true in a precise, mathematical sense is not all that relevant. The relevant question is how much variability is still possible in the MoI value once gravity is measured to realistic order and with realistic precision. Our answer, if this sample is representative, is: about 0.1% (but see below for the importance of rotation period uncertainty).

3.5. Rotation and gravity

A planet’s rotation period may be estimated by a variety of methods (e.g. Read et al. 2009; Helled et al. 2015; Gurnett et al. 2007; Mankovich et al. 2019; Anderson & Schubert 2007, and references therein) and with varying degrees of precision. In an example of a best case scenario, Jupiter’s deep interior rotation is tied to the precession of the polar axis of its strong magnetic field which can be measured to sub-second precision (Seidelmann et al. 2007). In other cases we are not so lucky; the

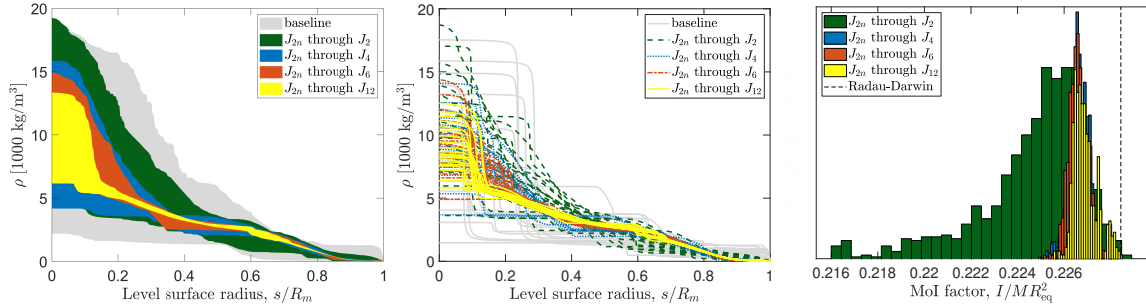


Figure 7. Same views as Fig. 5 showing samples constrained with successively higher order J_n up to J_{12} (n_{\max} in eq. 3), in addition to the constraints of mass, radius, and rotation period. The likelihood function used $\sigma_{J_2}/J_2 = 10^{-6}$, $\sigma_{J_4}/J_4 = 10^{-5}$, $\sigma_{J_6}/J_6 = 10^{-4}$, $\sigma_{J_8}/J_8 = 10^{-4}$, $\sigma_{J_{10}}/J_{10} = 10^{-2}$, and $\sigma_{J_{12}}/J_{12} = 10^0$.

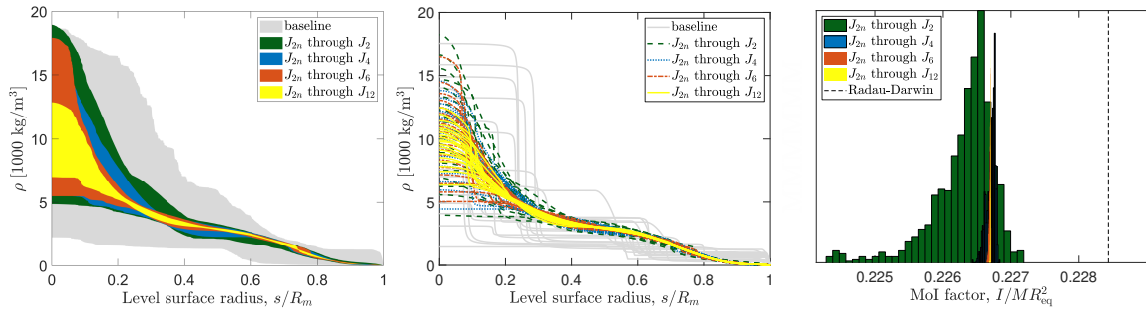


Figure 8. Same views as Fig. 7 showing samples obtained with a constant, rather than sampled, rotation period. (Note changed horizontal axis limits in MoI histogram.)

rotation periods of Uranus and Neptune are estimated with uncertainty of at least 10 minutes (in each direction) (Podolak & Helled 2012; Helled et al. 2010) and perhaps much higher.

In section 3.2 above we concluded that shrinking the uncertainty in the rotation period by itself does little to further constrain the space of allowable density profiles. However the same is not true when gravity is considered also. Figure 8 shows a sample obtained assuming a precisely known rotation period. Compare with Figure 7. The constraining power of gravity is significantly enhanced by precise knowledge of rotation. Or, said another way, ignoring uncertainty in rotation may lead to unjustifiably tight constraints being deduced from models. Assuming a precisely known rotation period⁴ is a common, though not universal simplification made by modelers. We caution that such a simplifying assumption should be carefully justified or, better yet, avoided.

As evident from the right panel of Figure 8, when both gravity and rotation period are known to high precision, the remaining variation in MoI value all but disappears (sample $\sigma/\mu \approx 10^{-5}$). An independent measurement of the MoI would have to be

⁴ Actually most models, including ours, prefer to fix a dimensionless rotation parameter such as $m = \omega^2 s_0^3 / GM$ where $\omega = 2\pi/P$ and s_0 is the 1-bar level surface mean radius. This is *almost* equivalent to fixing the rotation period P itself, but as the equilibrium shape and with it s_0 are allowed to change, one cannot keep the mass, equatorial radius, rotation period, and rotation parameter all fixed simultaneously. Normally benign, this subtlety can cause confusion when directly comparing models derived by different groups.

extremely precise if it is expected to distinguish between different models already fitting the other constraints.

3.6. Pressure-density relation

The density profile, $\rho(s)$, was the focus of our attention because it is the quantity that directly determines the gravity field, and is therefore directly inferred by its measurement. But the density itself is not really what we are most interested in. What we would like to know, ultimately, is what the planet is made of, its composition, and how the various molecular species are distributed inside the planet.

Gravity by itself can never give us this information, without additional information and/or assumptions. But it can get us a step closer by noting that the condition of hydrostatic equilibrium defines a one-to-one relationship between density and pressure, once the gravity field is known. If everywhere in the planet the weight of a layer of fluid is exactly balanced by the force due to pressure gradient, ∇p , then

$$\nabla p = -\rho \nabla U \quad (6)$$

everywhere, where U is the total potential, gravitational plus centrifugal. Note that U must be known in the interior of the planet, while the measured J_n values only relate to the external potential. Luckily, the process of calculating the external potential from a given $\rho(s)$ and rotation period also furnishes the potential on interior level surfaces as a useful byproduct. We can integrate, numerically, eq. (6) starting from the 1-bar reference level and obtain $p(s)$ and therefore $p(\rho)$ on every level surface.

The pressure-density relation, also called a *barotrope*, is not quite enough to uniquely relate to composition (a true equation-of-state would require the temperature profile as well) but it can already help by setting some bounds. Figure 9 shows the distribution envelope of barotropes integrated from the Uranus density profiles of Figures 7 and 8. The left panel corresponds to samples obtained with our conservative, $\sigma = 10$ min prior on rotation period, and the right panel corresponds to samples obtained with a precisely known rotation period. Adiabats of several compositions, computed with the SCvH and ANEOS equations of state (Saumon et al. 1995; Thompson 1990) are overlain for comparison.⁵ (The dotted line approximates a high metallicity envelope by adding water to the H/He adiabat at $Z = 0.57$ mass fraction, or about 100 times the solar O:H abundance.)

We see in Figure 9 how progressively higher-order gravity is able to shrink the allowable region in ρ - p space. The mass and radius of the planet (grey, baseline region) already tell us something about the possible composition; for example that Uranus is not dense enough to have a significant iron core. The low-order J_2 and J_4 , if measured with higher precision, can be used to narrow down further possible configurations, and higher-order J_n would help even more. But a precise determination of the underlying rotation period is necessary for maximum benefit.

⁵ The plots begin at 10 bars because the SCvH equation of state table does not extend down to the required temperature at 1 bar.

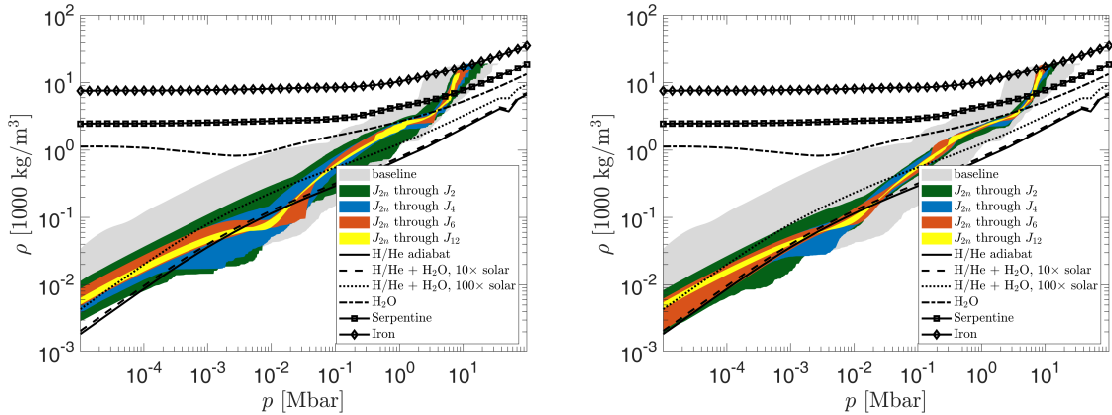


Figure 9. Pressure-density envelopes integrated from sampled $\rho(s)$ profiles of Uranus. *Left:* samples obtained with Gaussian prior on rotation period; *Right:* samples obtained with known rotation period. Overlain isentropes for hypothetical homogeneous compositions extend from a common $T_{10\text{bar}} = 150$ K.

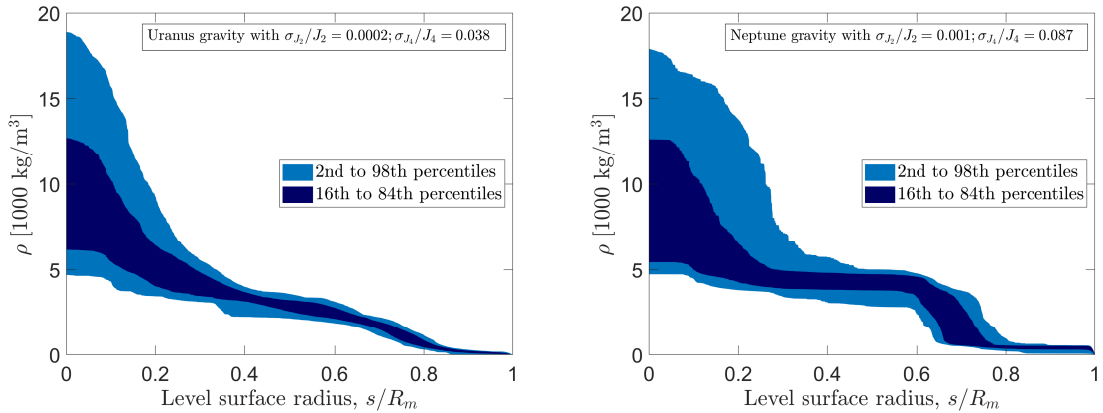


Figure 10. Envelope view of sampled $\rho(s)$ profiles of Uranus (left) and Neptune (right) matching currently available observables (Jacobson 2009, 2014). The dark shaded regions show the range of density value at every radius that lie between the 16th and 84th percentiles (roughly the sample’s “one sigma” spread) and the light shaded regions show value between the 2nd and 98th percentiles, roughly the sample’s “two sigma” spread.

4. REALISTIC CONSTRAINTS ON URANUS AND NEPTUNE

4.1. Constraints with presently known gravity

In the previous section we investigated the ability of gravity field measurements, in general, to constrain the interior density distribution of a fluid planet. We used nominal values of mass, radius, and low-order J s for Uranus to illustrate the results but the models presented above should not be used for making predictions about the real planet Uranus, since they use hypothetical uncertainty values. In this section we look at samples of interior models obtained with presently available best values and uncertainties for both Uranus and Neptune. We use the same views of the resulting distributions as in section 3 but showing side by side the same view for both planets.

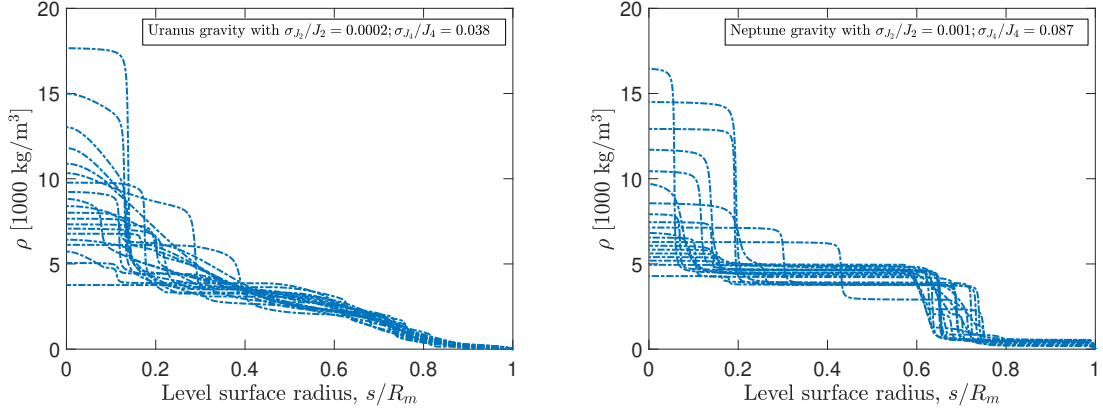


Figure 11. Ensemble view of sampled $\rho(s)$ profiles of Uranus (left) and Neptune (right) matching currently available observables.

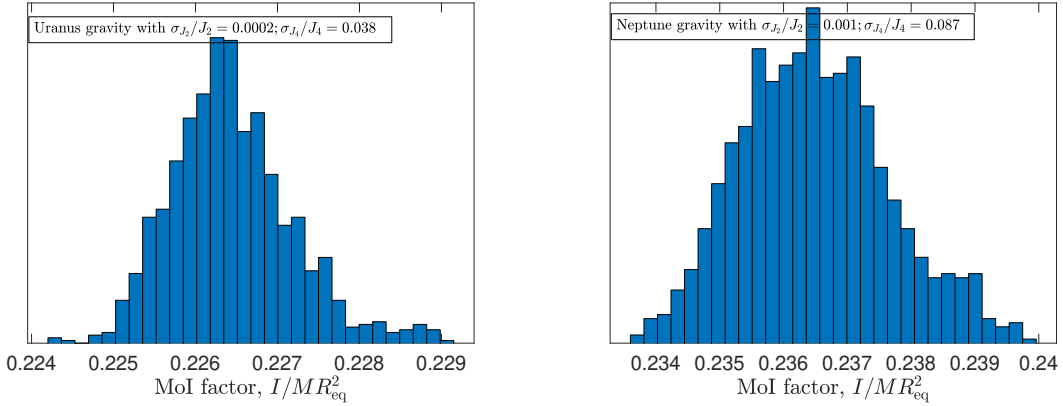


Figure 12. Moment of inertia factor histograms from sampled profiles of Uranus (left) and Neptune (right) matching currently available observables.

Figure 10 compares the planets in envelope view. The more accurately determined gravity of Uranus, compared with that of Neptune (Table 1) allows a much tighter constraint of density in the upper envelope but, as expected, does not help with the deep interior. A similar picture is evident with the ensemble view, Figure 11, while the MoI histograms in Figure 12 allow a prediction: the range of possible values of moment of inertia factor, should it ever be independently measured, is $0.225 \lesssim I/MR^2 \lesssim 0.229$ for Uranus, and $0.234 \lesssim I/MR^2 \lesssim 0.239$ for Neptune.

The barotrope view, Figure 13, allows us to make some statements about the planets' compositions, albeit only very generally. Both planets are too dense to *not* include significant amounts of heavy elements. No surprise there. But it seems that Neptune's entire envelope must be enriched with He or heavier elements, while a large (in pressure) fraction of Uranus is consistent with a solar composition H/He mixture, or even a somewhat helium poor atmosphere. This dichotomy is consistent with the one found in the models of [Nettelmann et al. \(2013, their Table 2\)](#), where the envelope of both planets was assumed to have a constant H/He ratio and much higher metallicity

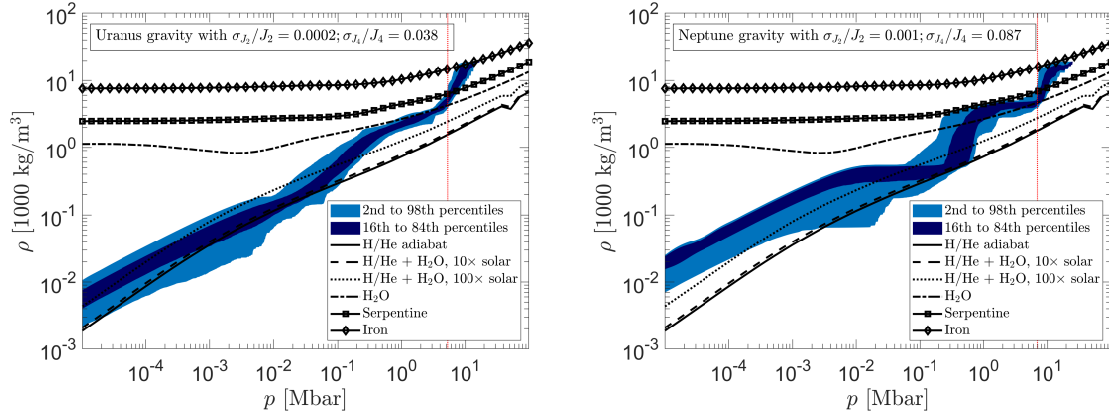


Figure 13. Barotrope view of sampled profiles of Uranus (left) and Neptune (right) matching currently available observables. The thin vertical line marks the sample’s minimum value of central pressure.

was required in Neptune’s envelope compared with Uranus. Observational constraints on the atmospheric abundances in both planets, from spectral data, are inconclusive, showing similar C:H ratios in both planets, for example, but detecting signatures of CO and HCN in the atmosphere of Neptune but not of Uranus (Gautier et al. 1995). Clearly, this would be one of the more important observations to improve upon should the opportunity arise.

It also appears, from Figure 13, that both planets allow for significant amounts of molecules heavier than water in their central regions, suggesting the existence of rocky cores. While the above interpretations are admittedly loose, and can probably be made more robust by comparisons with additional adiabatic and non-adiabatic barotropes of different compositions, they have the benefit of not being strongly model dependent. No assumptions at all about composition or temperature profile were made in obtaining the samples, and hence the blue shaded areas in Figure 13. The generality of the solutions is limited only by the flexibility of the parameterization, eq. (2.2), and the thoroughness of the sampling procedure (appendix A), and the implicit assumptions of hydrostatic equilibrium and rigid rotation at a well-known rotation rate.

4.2. A realistic scenario for future tight gravity field constraints

In sec. 2.5 we discussed how making use of high-order gravity, J_n^{obs} , would be impossible without some robust estimate of the effect of non-rigid rotation, J_n^{wind} . For this reason we obtained one more sample, for each planet, with the assumption of well known J_2 , J_4 , J_6 , and rotation period P , but unknown J_n for $n > 6$. These constraints correspond to a plausible scenario in which a future mission is able to obtain high-precision gravity and rotation period but uncertainty about the effects of deep zonal winds renders the higher order J_n unusable. This is similar to the current situation for Saturn where large differential rotation strongly affects the even J_n

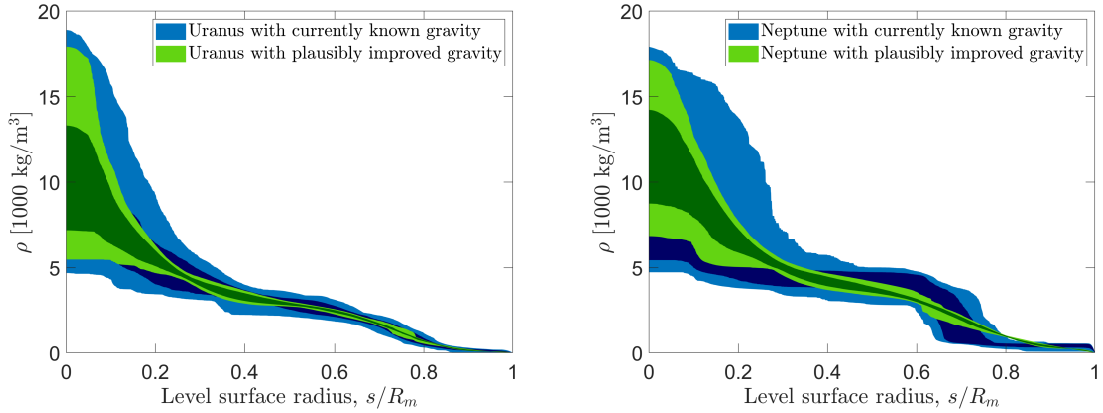


Figure 14. Envelope view of Uranus (left) and Neptune (right). Green shaded areas are samples obtained with the constraints of the scenario of sec. 4.2, showing the 1-sigma (dark green) and 2-sigma (light green) sample range, and overlain on the samples of Fig. 11 (blue) for comparison.

deduced from *Cassini* Grand Finale data and dynamical wind models must therefore be used to predict a J_n^{wind} correction (Iess et al. 2019).

With such a data set, how would our knowledge of the interior density profile for either Uranus or Neptune be improved? We find the improvement would be quite significant. Figure 14 shows the sampled profiles of density vs. radius, while Figure 15 shows density vs. pressure, which is potentially the most illustrative.

There are several aspects to note. In particular, the metallicity of the outer H/He envelope ($P < 0.1$ Mbar) could potentially be reliably assessed, given any consistency or inconsistency with a solar metallicity H/He adiabatic density profile. In addition, a metallicity enhancement that would deviate from a uniform enhanced metallicity could potentially be “seen” with gravity data. This would be more readily done at higher metallicities that deviate strongly from solar.

The long-standing question of whether the “middle” layers of Uranus and Neptune are exclusively made of water and other “ices”, or instead have less water but more H/He and rocks to give a similar density, may not be answerable, directly. However, the pressures at which changes in density structures occur, and the “slope” in density vs. pressure space of density profiles may well allow for plausible explanations for any constrained density profiles to be determined. Such profiles could be connected directly to predicted composition profiles from planet formation (Helled & Stevenson 2017; Ormel et al. 2021) and thermal evolution models (Vazan & Helled 2020; Scheibe et al. 2021; Stixrude et al. 2021). Clearly, the constraints on interior models would not only become much tighter than possible with currently available data but also tight enough in absolute terms to distinguish between different temperature/composition profiles.

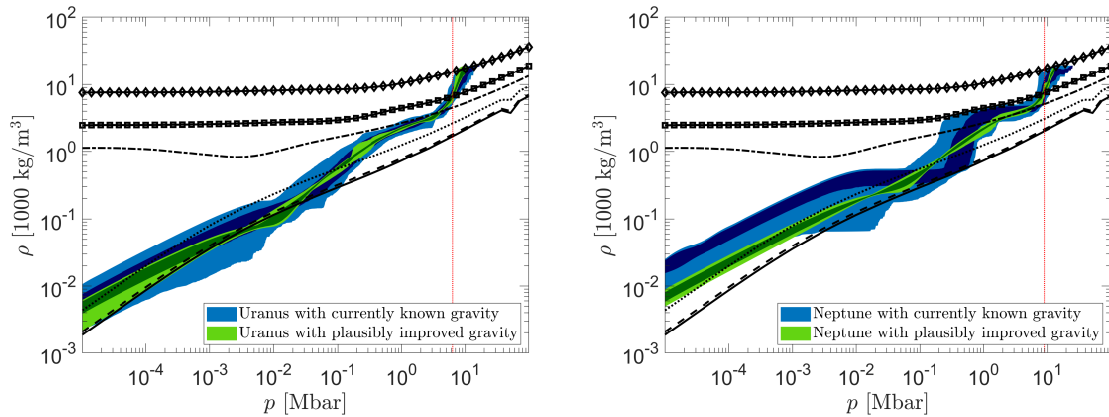


Figure 15. Barotrope view of Uranus (left) and Neptune (right). Green shaded area are samples obtained with the constraints of the scenario of sec. 4.2, showing the 1-sigma (dark green) and 2-sigma (light green) sample range, and overlain on the samples of Fig. 13 (blue) for comparison. The thin vertical line marks the improved sample's minimum value of central pressure.

5. SUMMARY AND CONCLUSIONS

In the previous sections we described an experiment designed to gauge the ability of a precise measurement of a planet's gravity to constrain the possible distribution of mass in its interior. Gravity is a long range force and the planet's gravitational potential at any exterior point is determined by an integral of the mass density over the entire planet so that, in principle, knowledge of one should inform on the other. In practice the gravitational potential can be measured with varying degrees of uncertainty: crudely, with the aid of natural satellites; better by tracking a flying-by spacecraft; with potentially exquisite precision by a dedicated orbiting mission. There is no simple formula connecting the degree of precision of the observed gravity, described by a set of expansion coefficients J_n and associated uncertainty σ_{J_n} , with the degree of constraint on the implied density distribution $\rho(s)$. Our main goal was to provide this connection by generating samples from the space of allowable $\rho(s)$ limited by successively higher order and higher precision gravity coefficients.

Examining the samples presented in sec. 3 led us to the conclusions summarized below. Many of these are unsurprising, being predictable at least qualitatively from the nature of the gravity integral. Nevertheless we find useful the more direct and more quantitative demonstration made possible by the sampling framework.

1. Even the most crude estimation of a planet's gravitational potential, say a measurement of only the J_2 coefficient to within one percent (Fig. 5) narrows down considerably the space of allowable density profiles, compared with a baseline constrained only by the planet's mass, radius, and boundary conditions. This narrowing down is most evident in the upper ten to twenty percent (by radius) of the planet's interior, very quickly disappearing with depth.

2. The degree of constraint applied to the interior $\rho(s)$ by a gravity measurement (a set of $J_n, \sigma_{J_n}, n \leq n_{\max}$) can be loosely quantified by the width of the distribution of associated moment of inertia values, a scalar quantity integrated from (and sensitive to!) $\rho(s)$ over the equilibrium shape of the planet.
3. More precisely known values of the low-order gravity coefficients are not nearly as useful as adding even crudely measured values of higher-order coefficients. Compare figures 5 and 7 and especially the rightmost panel in each. This fact presents a difficulty however, as higher-order coefficients are increasingly sensitive to, eventually dominated by dynamic effects not captured by simple rigid rotation rate, such as zonal winds and deep differential rotation. To be useful, these dynamic effects must be accounted for.
4. If high precision or high order gravity is to be used to constrain interior models then the planet's rotation period *must* also be known to comparable precision. Compare figures 7 and 8. This point is worth emphasizing since neglecting the uncertainty in rotation period can lead to overly confident predictions.
5. No level of precision and completeness of characterization of the gravity field and rotation state can be expected to pin down, by itself, the density at the center of a planet. Figure 8, yellow shaded area. To do better than a factor of two or more will require making additional assumptions.
6. A measurement of a planet's moment of inertia factor, in addition to and independent of the gravity field measurement, can potentially assist with constraining the interior mass distribution, but it would have to be a quite precise one. When only the low-order J_2 and J_4 are known and only to rough precision, as is the case presently for Uranus and Neptune, the distribution of the correlated MoI values is already constrained to a large degree: about 0.6% in the case of Uranus and about 1% for Neptune. If higher order J_n become known (and recall that this implies also precise determination of the rotation period) then the MoI is essentially fixed and can provide no further information.

A second goal of this work was to look at the presently available gravity field estimate of the planets Uranus and Neptune and see what predictions can be made about their interiors that would be, as much as possible, immune to implicit model assumptions and to uncertainties in the equations of state of Hydrogen, Helium, and heavier elements. Unsurprisingly, these predictions are general in nature and cannot replace detailed models. Nevertheless they illustrate the potential of more complete characterization of the gravity fields, should one become available, to better direct such models.

1. As is well known, both Uranus and Neptune are much too dense to *not* include significant quantities of elements heavier than helium. In their central regions,

both planets appear to allow significant enrichment by components denser than H_2O . To say anything more about the denser components will require a fuller characterization of the gravity field or making more detailed model assumptions or, very likely, both.

2. A fraction of Uranus' envelope is consistent with an adiabatic region of H/He at solar atmospheric abundances. Neptune's envelope however is not, and should be significantly metal-enriched or perhaps, somehow, He-rich.
3. An orbiter mission to better characterize the gravity field and rotation of either or both planets would be of very high value. Even if high-order gravity ($J_{n>6}$) cannot be reliably separated into hydrostatic and dynamic parts, the interior barotrope (density vs. pressure profile) could be tightly constrained. This would allow for direct comparisons of profiles of composition vs. depth from formation and evolution models, opening a new era into our understanding of Uranus and Neptune.

We would like to acknowledge the support of NSF grant AST 1908615 and NASA grant 80NSSC19K1286. Resources supporting this work were provided by the *lux* supercomputer at UC Santa Cruz, funded by NSF MRI grant AST 1828315. We thank two anonymous reviewers for the thorough reading of the manuscript and insightful comments.

APPENDIX

A. SAMPLING PROCEDURE

To draw a sample of $\rho(s)$ profiles for each planet we run the ensemble sampler of the `emcee` Python package (Foreman-Mackey et al. 2013) which implements the parallel stretch-move algorithm of Goodman & Weare (2010). The goal is a draw of a large enough sample of independent realizations of the model parameters (eq. 4) from the probability distribution dictated by the likelihood function (eq. 3), for each combination of observables and uncertainties (n_{max} and ν_n).

A.1. Variable transformations

In practice, sampling is often preceded by some isomorphic transformation of the physical model parameters into equivalent random variables whose probability distribution is predicted to be, in some sense, smoother and thus easier for the sampling algorithm to work with. The particular transformations are determined by analysis or, more often, by trial-and-error or by advice or general common wisdom suggestions. In the best cases a simple transformation, for example using a logarithm of a nondimensionlized variable, can lead to huge gains in efficiency. Even in the worst

Table 2. Sampling space parameters and their priors

physical parameter (eq. 4)	prior	sampling parameter	prior
z_1	$U(0.05, 0.5)$	$y_1 = \text{logit}(z_1)$	$\propto (e^y)/(1 + e^y)^2 \cdot U(\text{logit}(0.05), \text{logit}(0.5))$
σ_1	$U(0, \rho_{\max})$	$y_2 = \ln(\sigma_1)$	$\propto (e^y) \cdot U(-20, \ln(\rho_{\max}))$
ν_1	$U(20, 1000)$	$y_3 = \ln(\nu_1)$	$\propto (e^y) \cdot U(\ln(20), \ln(1000))$
z_2	$U(0.5, 0.85)$	$y_4 = \text{logit}(z_2)$	$\propto (e^y)/(1 + e^y)^2 \cdot U(\text{logit}(0.5), \text{logit}(0.85))$
σ_2	$U(0, \rho_{\max})$	$y_5 = \ln(\sigma_2)$	$\propto (e^y) \cdot U(-20, \ln(\rho_{\max}))$
ν_2	$U(20, 1000)$	$y_6 = \ln(\nu_2)$	$\propto (e^y) \cdot U(\ln(20), \ln(1000))$
a_8, a_7, \dots, a_2	$U(-10^7, 10^7)$	y_7, y_8, \dots, y_{13}	$U(-10^7, 10^7)$

$$\text{logit}(x) = \ln(x) - \ln(1 - x)$$

transformed priors conserve probability mass: $p(x)dx = p(y)dy$

cases these transformations are always benign (barring any programming bugs or math errors) so they are often left unmentioned in publication, but in order to facilitate exact reproducibility here we give the exact parameters used by the sampling algorithm. Table 2 defines the correspondence between the physical-space parameters (eq. 4, reproduced here for convenience) and the sample-space parameters explored by the MCMC chains. We make no claim that these are optimal or necessary.

$$\rho(z) = \rho(s/R_m) = \sum_{n=2}^8 a_n(z^n - 1) + \rho_0 + \sum_{n=1}^2 \frac{\sigma_n}{\pi} \left(\frac{\pi}{2} + \arctan(-\nu_n(z - z_n)) \right). \quad (\text{A1})$$

A.2. Seeds

In theory the seeds used to initiate the walkers of the ensemble sampler are completely unimportant, as each chain is assumed to run long enough to fully “forget” its initial state. A simple choice was to seed all walkers with the simplest possible density profile consistent with the planet’s mass and radius. This would be, in our parameterization, something like

$$\mathbf{y} = (0, -20, 100, 0, -20, 100, 0, 0, 0, 0, 0, \frac{5}{2}\rho_0 - \frac{15}{8\pi} \frac{M}{R^3}). \quad (\text{A2})$$

These values create a single quadratic in $z = r/R_m$ starting at $\rho = \rho_0$ at the surface and implying, for a spherical planet of radius R , a total mass M . Starting the sampling from this bland, featureless seed the likelihood function should produce density profiles with interesting features (i.e. steeper gradients and sharp discontinuities) if and where they are “preferred” by the data. This is, in fact, exactly what happens, very slowly. The mixing rate between walkers in our samples is very low, probably due to correlations between parameters.

In order to speed up the generation of new samples we save and reuse density profiles (parameter values) from already generated samples. A new ensemble of n_w walkers

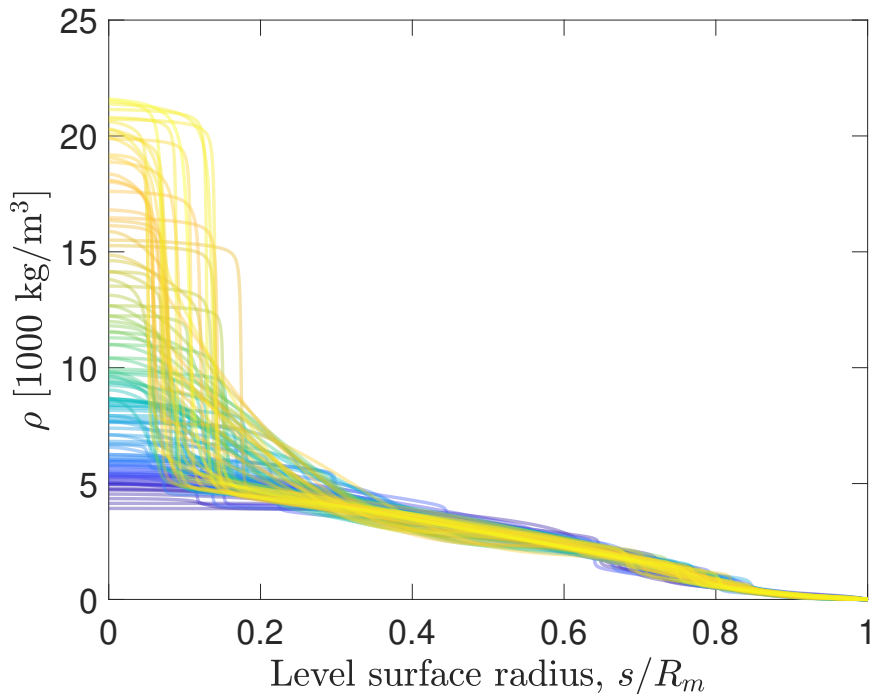


Figure 16. Density profiles of a typical ensemble seed state.

is seeded with a random choice of n_w items from a large seed bank of diverse profiles, and may start out looking like the example in Figure 16. While this doesn't solve the problem of slow mixing, once the chains are long enough to forget their initial state (longer than their autocorrelation time) the final links from each chain are an independent sample of size n_w .

A.3. Tempering

To improve inter-walker mixing we use a common idea known as tempering. The ensemble is run for a while under an artificially widened likelihood function, designed to lower the peaks and raise the valleys in the likelihood landscape. In our case this is equivalent to assuming very poorly known values for the planet's observables (gravity, mass, rotation period). Under this likelihood function walkers can readily mix and do not get stuck in local regions of high likelihood. After a few autocorrelation times (much shorter now) the ensemble walkers are well mixed and are spread out in parameter space following the posterior distribution, but of the modified likelihood. When the real likelihood is then applied, this effectively creates an ideal seed state for the ensemble. When the walkers then continue under the real likelihood they explore their local neighborhood more slowly, and would get stuck if they find a high-likelihood peak. But at this point the last link from each walker is collected and the process restarts, repeating the cycle as many times as necessary to produce a final sample of 1000 independent states.

We believe but did not mathematically prove that this procedure satisfies the requirement of detailed balance, which makes it an MCMC algorithm and guarantees

that each $\rho(s)$ appears in the final sample in proportion to its frequency in the unknown posterior distribution. More important for the purpose of this work, however, is that the procedure is able to efficiently explore the entire parameter space.

REFERENCES

- Anderson, J. D., & Schubert, G. 2007, *Science* (80-.), 317, 1384, doi: [10.1126/science.1144835](https://doi.org/10.1126/science.1144835)
- Bailey, E., & Stevenson, D. J. 2021, *Planet. Sci. J.*, 2, 64, doi: [10.3847/PSJ/abd1e0](https://doi.org/10.3847/PSJ/abd1e0)
- Bolton, S., Adriani, A., Adumitroaie, V., et al. 2017, *Science* (80-.), 356, 821, doi: [10.1126/science.aal2108](https://doi.org/10.1126/science.aal2108)
- Debras, F., & Chabrier, G. 2017, *A&A*, 97, doi: [10.1051/0004-6361/201731682](https://doi.org/10.1051/0004-6361/201731682)
- Durante, D., Parisi, M., Serra, D., et al. 2020, *Geophys. Res. Lett.*, 47, doi: <https://doi.org/10.1029/2019GL086572>
- Fletcher, L. N., Helled, R., Roussos, E., et al. 2020, *Planet. Space Sci.*, 191, 105030, doi: <https://doi.org/10.1016/j.pss.2020.105030>
- Foreman-Mackey, D., Hogg, D. W., Lang, D., & Goodman, J. 2013, *Publ. Astron. Soc. Pacific*, 125, 306, doi: [10.1086/670067](https://doi.org/10.1086/670067)
- Galanti, E., & Kaspi, Y. 2017, *Astrophys. J.*, 843, L25, doi: [10.3847/2041-8213/aa7aec](https://doi.org/10.3847/2041-8213/aa7aec)
- Galanti, E., Kaspi, Y., Miguel, Y., et al. 2019, *Geophys. Res. Lett.*, 616, doi: [10.1029/2018GL078087](https://doi.org/10.1029/2018GL078087)
- Gautier, D., Conrath, B. J., Owen, T., de Pater, I., & Atreya, S. K. 1995, in *Neptune Trit.*, 547–612
- Goodman, J., & Weare, J. 2010, *Commun. Appl. Math. Comput. Sci.*, 5, 65
- Gurnett, D. A., Persoon, A. M., Kurth, W. S., et al. 2007, *Science* (80-.), 316, 442, doi: [10.1126/science.1138562](https://doi.org/10.1126/science.1138562)
- Helled, R. 2011, *Astrophys. J. Lett.*, 735, doi: [10.1088/2041-8205/735/1/L16](https://doi.org/10.1088/2041-8205/735/1/L16)
- Helled, R., Anderson, J. D., Podolak, M., & Schubert, G. 2011a, *Astrophys. J.*, 726, doi: [10.1088/0004-637X/726/1/15](https://doi.org/10.1088/0004-637X/726/1/15)
- Helled, R., Anderson, J. D., & Schubert, G. 2010, *Icarus*, 210, 446, doi: [10.1016/j.icarus.2010.06.037](https://doi.org/10.1016/j.icarus.2010.06.037)
- Helled, R., Anderson, J. D., Schubert, G., & Stevenson, D. J. 2011b, *Icarus*, 216, 440, doi: [10.1016/j.icarus.2011.09.016](https://doi.org/10.1016/j.icarus.2011.09.016)
- Helled, R., & Fortney, J. J. 2020, *Philos. Trans. R. Soc. A Math. Phys. Eng. Sci.*, 378, doi: [10.1098/rsta.2019.0474](https://doi.org/10.1098/rsta.2019.0474)
- Helled, R., Galanti, E., & Kaspi, Y. 2015, *Nature*, doi: [10.1038/nature14278](https://doi.org/10.1038/nature14278)
- Helled, R., Nettelmann, N., & Guillot, T. 2020, *Space Sci. Rev.*, 216, 38, doi: [10.1007/s11214-020-00660-3](https://doi.org/10.1007/s11214-020-00660-3)
- Helled, R., Schubert, G., & Anderson, J. D. 2009, *Icarus*, 199, 368, doi: [10.1016/j.icarus.2008.10.005](https://doi.org/10.1016/j.icarus.2008.10.005)
- Helled, R., & Stevenson, D. J. 2017, *Astrophys. J. Lett.*, 840, L4, doi: [10.3847/2041-8213/aa6d08](https://doi.org/10.3847/2041-8213/aa6d08)
- Hofstadter, M., Simon, A., Atreya, S., et al. 2019, *Planet. Space Sci.*, 177, 104680, doi: [10.1016/j.pss.2019.06.004](https://doi.org/10.1016/j.pss.2019.06.004)
- Hubbard, W. 2013, *Astrophys. J.*, 768, 43
- Hubbard, W. B. 2012, *Astrophys. J. Lett.*, 756, L15, doi: [10.1088/0004-637X/768/1/43](https://doi.org/10.1088/0004-637X/768/1/43)
- Hubbard, W. B., Schubert, G., Kong, D., & Zhang, K. 2014, *Icarus*, 242, 138, doi: [10.1016/j.icarus.2014.08.014](https://doi.org/10.1016/j.icarus.2014.08.014)
- Iess, L., Folkner, W. M., Durante, D., et al. 2018, *Nature*, 555, 220, doi: [10.1038/nature25776](https://doi.org/10.1038/nature25776)
- Iess, L., Militzer, B., Kaspi, Y., et al. 2019, *Science* (80-.), 2965, eaat2965, doi: [10.1126/science.aat2965](https://doi.org/10.1126/science.aat2965)
- Jacobson, R. 2014, *Astron. J.*, 148, 76, doi: [10.1088/0004-6256/148/5/76](https://doi.org/10.1088/0004-6256/148/5/76)
- Jacobson, R. A. 2009, *Astron. J.*, 137, 4322, doi: [10.1088/0004-6256/137/5/4322](https://doi.org/10.1088/0004-6256/137/5/4322)

- Kaspi, Y., Showman, A. P., Hubbard, W. B., Aharonson, O., & Helled, R. 2013, *Nature*, 497, 344, doi: [10.1038/nature12131](https://doi.org/10.1038/nature12131)
- Kaspi, Y., Guillot, T., Galanti, E., et al. 2017, *Geophys. Res. Lett.*, 44, 5960, doi: [10.1002/2017GL073629](https://doi.org/10.1002/2017GL073629)
- Kaspi, Y., Galanti, E., Hubbard, W. B., et al. 2018, *Nature*, 555, 223, doi: [10.1038/nature25793](https://doi.org/10.1038/nature25793)
- Lindal, G. F. 1992, *Astrophys. J.*, 103, 967, doi: [10.1086/116119](https://doi.org/10.1086/116119)
- Mankovich, C. R., & Fortney, J. J. 2020, *Astrophys. J.*, 889, 51, doi: [10.3847/1538-4357/ab6210](https://doi.org/10.3847/1538-4357/ab6210)
- Mankovich, C. R., & Fuller, J. 2021, *Nat. Astron.*, doi: [10.1038/s41550-021-01448-3](https://doi.org/10.1038/s41550-021-01448-3)
- Mankovich, C. R., Marley, M. S., Fortney, J. J., & Movshovitz, N. 2019, *Astrophys. J.*, 871, 1, doi: [10.3847/1538-4357/aaf798](https://doi.org/10.3847/1538-4357/aaf798)
- Marley, M. S., Gomez, P., & Podolak, M. 1995, *J. Geophys. Res.*, 100, 23,349, doi: [10.1029/95JE02362](https://doi.org/10.1029/95JE02362)
- Movshovitz, N., Fortney, J. J., Mankovich, C. R., Thorngren, D., & Helled, R. 2020, *Astrophys. J.*, 891, 109, doi: [10.3847/1538-4357/ab71ff](https://doi.org/10.3847/1538-4357/ab71ff)
- Nelson, B. E., Ford, E. B., Buchner, J., et al. 2018, Quantifying the Evidence for a Planet in Radial Velocity Data. <https://arxiv.org/abs/1806.04683>
- Nettelmann, N. 2017, *A&A*, 139, doi: [10.1051/0004-6361/201731550](https://doi.org/10.1051/0004-6361/201731550)
- Nettelmann, N., Helled, R., Fortney, J. J., & Redmer, R. 2013, *Planet. Space Sci.*, 77, 143, doi: [10.1016/j.pss.2012.06.019](https://doi.org/10.1016/j.pss.2012.06.019)
- Nettelmann, N., Movshovitz, N., Ni, D., et al. 2021, *Planet. Sci. J.*, 2, 241, doi: [10.3847/PSJ/ac390a](https://doi.org/10.3847/PSJ/ac390a)
- Neuenschwander, B. A., Helled, R., Movshovitz, N., & Fortney, J. J. 2021, *Astrophys. J.*, 910, 38, doi: [10.3847/1538-4357/abdfd4](https://doi.org/10.3847/1538-4357/abdfd4)
- Ormel, C. W., Vazan, A., & Brouwers, M. G. 2021, *Astron. Astrophys.*, 647, doi: [10.1051/0004-6361/202039706](https://doi.org/10.1051/0004-6361/202039706)
- Podolak, M., & Helled, R. 2012, *Astrophys. J.*, 759, L32, doi: [10.1088/2041-8205/759/2/L32](https://doi.org/10.1088/2041-8205/759/2/L32)
- Podolak, M., Podolak, J., & Marley, M. 2000, *Planet. Space Sci.*, 48, 143, doi: [10.1016/S0032-0633\(99\)00088-4](https://doi.org/10.1016/S0032-0633(99)00088-4)
- Read, P. L., Dowling, T. E., & Schubert, G. 2009, *Nature*, 460, 608, doi: [10.1038/nature08194](https://doi.org/10.1038/nature08194)
- Rymer, A. M., Runyon, K. D., Clyde, B., et al. 2021, *Planet. Sci. J.*, 2, 184, doi: [10.3847/PSJ/abf654](https://doi.org/10.3847/PSJ/abf654)
- Saumon, D., Chabrier, G., & van Horn, H. M. 1995, *Astrophys. J. Suppl.* v.99, 99, 713, doi: [10.1086/192204](https://doi.org/10.1086/192204)
- Scheibe, L., Nettelmann, N., & Redmer, R. 2021, *Astron. Astrophys.*, 650, A200, doi: [10.1051/0004-6361/202140663](https://doi.org/10.1051/0004-6361/202140663)
- Seidelmann, P. K., Archinal, B. A., A'Hearn, M. F., et al. 2007, *Celest. Mech. Dyn. Astron.*, 98, 155, doi: [10.1007/s10569-007-9072-y](https://doi.org/10.1007/s10569-007-9072-y)
- Stevenson, D. J. 2020, *Annu. Rev. Earth Planet. Sci.*, 48, 465, doi: [10.1146/annurev-earth-081619-052855](https://doi.org/10.1146/annurev-earth-081619-052855)
- Stevenson, D. J., & Salpeter, E. E. 1977, *Astrophys. J. Suppl. Ser.*, 35, 221
- Stixrude, L., Baroni, S., & Grasselli, F. 2021, *Planet. Sci. J.*, 2, 222, doi: [10.3847/PSJ/ac2a47](https://doi.org/10.3847/PSJ/ac2a47)
- Teanby, N. A., Irwin, P. G. J., Moses, J. I., & Helled, R. 2020, *Philos. Trans. R. Soc. A Math. Phys. Eng. Sci.*, 378, doi: [10.1098/rsta.2019.0489](https://doi.org/10.1098/rsta.2019.0489)
- Thompson, S. L. 1990, ANEOS Analytic Equations of State for Shock Physics Codes Input Manual, Tech. rep., Sandia National Laboratories, Albuquerque, New Mexico
- Tiesinga, E., Mohr, P. J., Newell, D. B., & Taylor, B. N. 2021, *Rev. Mod. Phys.*, 93, 7621, doi: [10.1103/RevModPhys.93.025010](https://doi.org/10.1103/RevModPhys.93.025010)
- Vazan, A., & Helled, R. 2020, *Astron. Astrophys.*, 633, 1, doi: [10.1051/0004-6361/201936588](https://doi.org/10.1051/0004-6361/201936588)
- Wisdom, J., & Hubbard, W. B. 2016, *Icarus*, 267, 315, doi: [10.1016/j.icarus.2015.12.030](https://doi.org/10.1016/j.icarus.2015.12.030)